RESEARCH ARTICLE

Infrared thermography investigations in transitional supersonic boundary layers

Simone Zuccher · William S. Saric

Abstract The study of boundary-layer transition in supersonic flows is conducted employing infrared thermography (IRT). Several models of swept wings are tested in a blow-down facility at Mach number 2.4. The effects of wing sweep and other parameters (angle of attack, leading-edge contour, presence/absence of surface roughness) are successfully observed. The transition front is clearly identified, demonstrating the utility of IRT for this type of study. The technique is particularly indicated for flows that are sensitive to surface alterations (roughness), such as transitional boundary layers, because it does not require interaction with the model or the flow under investigation. The additional advantage of no need for special apparatus, except for the infrared camera, makes IRT well suited for both wind-tunnel and in-flight testing. Practical problems and limitations encountered when dealing with IRT in high-speed flows are also discussed.

S. Zuccher · W. S. Saric
Department of Mechanical and Aerospace Engineering,
Arizona State University, Tempe, AZ 85287, USA
e-mail: zuccher@sci.univr.it

W. S. Saric
e-mail: saric@aeromail.tamu.edu

S. Zuccher (✉)
Department of Computer Science, University of Verona,
37134 Verona, Italy
e-mail: zuccher@sci.univr.it

Present Address:
W. S. Saric
Department of Aerospace Engineering, Texas A&M University,
College Station, TX 77843, USA

1 Motivations

1.1 Drag reduction in supersonic flight

The general goal of improving aircraft performance in supersonic flight is strictly related to drag reduction and laminar-to-turbulent boundary-layer transition. Because an airplane flying at high speed experiences drag originating from lift, shock waves, and skin friction, efficient drag reduction can be achieved only by understanding the physics of each contribution and by counter-acting it accordingly.

Lift-induced drag is due to the vorticity generated by a lifting wing, which takes the form of a strong vortex released at the wing tip. The consequent downwash and the dissipation of the vortex further downstream are responsible for energy losses. In subsonic and transonic flight this type of drag is typically controlled by using winglets or wings with large aspect ratios. In supersonic conditions, however, these remedies would result in stronger or additional shock waves. Therefore, the control of lift-induced drag in supersonic flight is practically impossible.

The so-called "wave drag" originates from a high-pressure region immediately downstream of shock waves. In the case of straight and blunt-nose wings, a detached bow shock forms upstream of the leading edge. If the wing is swept backwards, however, the pressure drop across the shock wave is reduced and so is the wave drag. Moreover, if the sweep angle is large enough to completely contain the leading edge within the Mach angle, the shock wave cannot originate and the wave drag can be limited to the pressure recovery region. Additional benefits, such as the reduction of sonic-boom effects in supersonic flight and the increase of critical Mach number in transonic flight, make swept wings particularly suited for high-speed applications.

Viscous drag (or skin-friction drag) concerns both low- and high-speed applications and is due to the shear stresses on the surfaces and in the boundary layer. The decreased momentum in the flowfield results in a corresponding loss of momentum of the aerodynamic system. As opposed to wave drag and drag due to lift, which can be reduced or suppressed by employing an appropriate wing geometry, viscous drag is more difficult to control because its origin can be various. The physical mechanism of laminar-to-turbulent boundary-layer transition is directly responsible, but shear layers and boundary-layer separation are also involved. At high Mach-number regimes, transition to turbulence causes further problems due to large heat loads induced by mixing enhancement typical of turbulent flows. Therefore, ensuring laminar flow over most of the wing of a modern supersonic airplane would result in remarkable engineering benefits related to both aerodynamic performances and structural design.

It is clear that the choice of wing geometry is a key feature in drag reduction and/or transition control. Because shock waves cause the largest amount of drag in supersonic flight, here we focus on swept-wings, possibly with subsonic leading edge. The latter, in fact, eliminates completely the upstream shock wave due to the wing. On the other hand, the swept-wing geometry is rather complex and allows many physical mechanisms of boundary-layer transition.

Despite the considerable efforts done insofar, the physics of transition in high-speed boundary layers is still poorly understood, partly due to lack of experiments. By showing some results in supersonic swept-wing flows, the present study aims at proposing infrared thermography (IRT) as a successful technique to easier this type of investigations.

1.2 Transition to turbulence in subsonic and supersonic swept-wing boundary layers

The classical view of the transition process in external boundary layers is predominantly centered around the slow linear amplification of exponentially growing disturbances (the familiar Tollmien–Schlichting waves), preceded by a receptivity process to the disturbance environment (Morkovin 1969) and followed by secondary instabilities, further nonlinearity and finally a breakdown to a recognizable turbulent flow (T–S path). This picture, however, had to be urgently reconsidered with the evidence of transition phenomena, labeled by Morkovin (1985) as "bypass transition", that could not be attributed to this T–S path, and with the emergence of a literature on transient growth in the early 1990s.

When swept wings are considered, the phenomenon of boundary-layer transition is further complicated by the fact

that the combination of four basic instability mechanisms can cause it (Saric et al. 2003), so that its control has to change accordingly. Görtler instabilities (Saric 1994) can develop on concave curvature surfaces and can be controlled by the appropriate profile design. Attachment-line contamination and instability (Pfenninger 1977; Poll 1985) can originate from improper values of leading-edge radius and sweep angle, and can be controlled by keeping them below a critical value. Streamwise instabilities related to the Tollmien–Schlichting mechanism, which typically occur in the mid-chord region (Reed et al. 1996), can be easily controlled using a favorable pressure gradient and by minimizing the extent of the pressure-recovery region. The favorable pressure gradients used to stabilize streamwise instabilities, however, have a negative effect on the crossflow instability (the fourth mechanism), which originates from an imbalance between centripetal acceleration and pressure gradient.

The present study focuses on the crossflow instability developing in supersonic swept-wing boundary layers. Regardless of the instability process, the first stage is always the receptivity mechanism, which allows external disturbances to enter the boundary layer and grow. Different excitation sources such as freestream turbulence, surface roughness, or their interaction, can play a significant role in the receptivity of 3-D boundary layers. For a detailed description of receptivity in incompressible flows the reader is referred to Saric et al. (2000). In a low-turbulence environment, such as flight conditions, experiments by Deyhle and Bippes (1996) showed that the transition mechanism is dominated by stationary crossflow waves. At large disturbance levels, traveling waves dominate and can overshadow the stationary structure because of the larger-amplitude, unsteady initial conditions.

Saric et al. (2003) report recent results regarding 3-D boundary-layer stability in the incompressible case and complement the review by Reed and Saric (1989) about the work done during the 1980s. Efforts specifically related to crossflow instability on swept wings and further references can be found in these two review papers.

Experimental and theoretical studies of stability and transition in supersonic 3-D boundary layers and swept wings are less numerous. Creel et al. (1987) investigated transition on a swept cylinders at Mach number $M = 3.5$ in the Langley quiet tunnel. King (1992) carried out experiments on transition in the 3-D boundary layer developing on a sharp cone at an angle of attack for $M = 3.5$. Levchenko et al. (1996) considered the evolution of natural fluctuations in the boundary layer on a swept wing. Mielke and Kleiser (1999) studied laminar-to-turbulent transition in a 3-D supersonic boundary layer by means of DNS. Kosinov et al. (2000) presented results of an experimental study in which controlled disturbances developed on a

swept-wing model at $M = 2$. Semisynov et al. (2003) reported some experimental investigations regarding the evolution of natural disturbances in the supersonic boundary layer developing on the attachment line of a circular cylinder with a sweep angle of $68°$ at $M = 2$.

Experiments similar to those reported in the present work were carried out by Cattafesta et al. (1995) on a swept wing at $M = 3.5$ and results compared with computations. Temperature-sensitive paints and a sublimating chemical were used to visualize surface flow features, such as transition location, and to provide qualitative insights. Quantitative measurements were performed using distributed thermocouples and surface (static) pressure ports. Experimental data were compared with mean-flow results computed employing the thin-layer Navier–Stokes equations, and N-factors calculated using the envelope e^N method. Traveling disturbances with $N = 13$ provided a good correlation with the transition data, while computed disturbances with frequencies in the range 40–60 kHz had the largest N factors. Results exhibit sharp pressure gradients close to the leading edge and transition fronts approximately parallel to it, indicating crossflow-dominated transition.

The main limitations of the work by Cattafesta et al. (1995), as clearly stated by the authors, were the detection of mean-flow quantities only and the lack of spatial resolution due to the use of a limited number of thermocouples. As they recognized, "This limitation [the lack of spatial resolution] is a drawback of the present methods and emphasizes the need for higher spatial-resolution transition-location measurement techniques for three-dimensional flows". We propose IRT as the technique to overcome this limitation.

2 Measurement techniques and flow visualizations for high-speed transition investigations

2.1 Some possible approaches

Boundary-layer transition in high-speed flows can be investigated by employing both quantitative and qualitative approaches. Temperature measurements carried out using thermocouples, static pressure measurements, temperature sensitive paints (TSP), pressure sensitive paints (PSP), phosphor thermography, liquid crystals and infrared thermography fall in the first group of quantitative techniques and provide local or global measurements of pressure and temperature. On the other hand, oil-flow visualizations and sublimating chemical methods can disclose interesting flow-features such as transition fronts and possible regions of separation on a relatively large portion of the model. Qualitative and quantitative methods are usually combined together to achieve a better understanding of the phenomenon under investigation, as done by Cattafesta et al. (1995) (surface pressure and temperature measurements together with oil-flow visualizations, sublimating chemical methods and TSP) or Matsumura and Schneider (2003) (TSP and fluorescent oil-flow visualization).

Pressure taps, which are normally used to measure the pressure coefficient C_p on the model, and thermocouples, which have high installation costs and limited spatial resolution (see limitations in Cattafesta et al. 1995), are accurate but local. On the contrary, TSP and PSP can provide quantitative information in a simpler and much cheaper way, allowing higher spatial resolution and full-field measurements (Liu et al. 1997). In general, TSP and PSP are prepared by dissolving a luminescent substance in a polymer solution and thus require not only spraying, brushing or dipping the surface but also a measurement system that includes illumination sources, optical filters, photodetectors and data acquisition/processing units along with the (nontrivial) calibration procedure.

Phosphor thermography has been utilized for the study of boundary-layer transition induced by crossflow and roughness in high-speed applications (Berry et al. 1997). This method requires a ceramic model coated with phosphors that fluoresce in two regions of the visible spectrum when illuminated with ultraviolet (UV) light. Temperature distributions are obtained with a color video camera. For complex models Merski (1999) proposed a weighted two-color relative-intensity technique. The fabrication of wind-tunnel models is a critical component of this technique because they need to be made of a material with low thermal diffusivity and well-defined, uniform, isotropic thermal properties. In addition to the fluorescent model, this technique requires the use of UV lights and color CCD camera (both located outside the wind tunnel), calibration and data reduction.

Surface visualization methods are qualitative and normally used to examine surface streamline patterns, vortex tracks, regions of separated flow, stationary crossflow disturbances and transition location. The most common approach utilizes small dots of oil to trace out the surface streamlines, but due to the required skill and patience this technique can be considered a bit of an art. To make the whole process faster (setting small dots of oil on the surface can be very time consuming), the oil can be spread evenly on the model but the large amount of oil on the surface makes the streamlines and reattachment lines hard to detect. Matsumura and Schneider (2003) improved the traditional technique by adding fluorescent pigmentation and using blue light to eliminate some reflections.

Sublimating chemicals have been used in subsonic and supersonic flows. Typically, chemical fluorine is dissolved in ethyl alcohol and then sprayed on the model surface.

When the alcohol evaporates, the fluorine is left on the model and during the run the chemical sublimes at a rate that is directly related to the local shear stress. Transition location and stationary crossflow disturbances can be easily identified (Cattafesta et al. 1995).

Other techniques, such as hotfilms and hotwire ane-mometry, are not discussed here. The reason is that we are looking for a method to identify transition possibly in only one run. These approaches are very good for localized investigations, but they need multiple runs in order to map the whole flow field over the model. It goes without saying that, once the transition front has been identified using a global technique, interesting details such as frequency of a possibly travelling wave or disturbance levels can be obtained only with hotfilms or hotwires.

2.2 Infrared thermography and its role in the present experiments

Infrared thermography is an alternative method to those described above for transition detection in high-speed flows.

The infrared energy radiating from the object under investigation is detected by the camera and, assuming that the emissivity is known, a map of the model surface tem-perature distribution can be obtained at once by employing the Stefan–Boltzmann law. Each temperature level, corre-sponding to a certain level in the radiated energy, is represented on the image by a different color or gray-scale level. For common applications the useful portion of the infrared spectrum lies in the range between 0.8 and 20 μm but the most useful bands are 3–5 μm (short waves) and 8–12 μm (long waves) because they match the atmospheric transmission bands. For operating distances restricted to a few meters, and in the absence of fog or water droplets, the atmospheric absorption has little effect (Maldague and Moore 2001).

Infrared thermography is particularly appealing and currently used in engineering because results are relatively easy to obtain and its span of applications is very wide. Besides being non-destructive and non-invasive, other valuable features are its high spatial resolution and fast response time, the fact that direct contact with the object is not needed and that the investigated area can be up to a few square meters at a time. Moreover, IRT can be a unique tool for some inspection tasks otherwise impossible, as in high-temperature environments (Kaplan 1999; Maldague 2001; Maldague and Moore 2001). On the other hand, IRT suffers from some drawbacks such as cost of the equip-ment, capability of detecting only phenomena resulting in a measurable change of the thermal properties, ability to inspect a limited thickness of material under the surface

(IRT is a "boundary" technique), and difficulty in knowing emissivity changes as a function of the position on the surface. All these factors, however, are not an issue in our experiments.

State-of-the-art infrared cameras are nowadays able to measure temperature differences with an accuracy of nearly 0.1 K over a small area. This improved resolution of details has made IRT a very powerful tool to visualize flow phenomena that produce measurable temperature changes on the model, such as shock waves, flow separation and laminar-to-turbulent boundary-layer transition. Infrared technology has been employed in wind-tunnel tests (Hall et al. 1991), and in-flight tests from subsonic to hypersonic conditions. For flight tests, both local and remote camera installations have been used. In the first case the camera and the model are on the same aircraft (Quast 1987; Brandon et al. 1990; Miley et al. 1997), while in "remote" installations the model and the camera are on different airplanes (Green et al. 1983; Van Dam et al. 1998; Blanchard and Tietjen 2000).

The basic principle behind the use of IRT for transition detection is the difference in the convective-heat-transfer coefficients between laminar and turbulent flows. The laminar boundary layer allows very low heat exchange between the model surface and the surrounding freestream flow, whereas the turbulent boundary layer features high mixing and thus high convective heat exchange. Therefore, laminar regions behave as an insulator when compared with turbulent regions. In practice, the portion of the sur-face beneath the laminar boundary layer keeps its initial temperature for a period of time longer than that of the surface beneath the turbulent boundary layer. Since the freestream flow is, in general, at a different temperature than the model, this results in two regions at different temperatures, separated by a line of sharp temperature gradient corresponding to the transition front. For a run at ambient temperature, the air is typically colder than the model because of adiabatic cooling and a lower recovery temperature. Therefore, a region of turbulent boundary layer appears as cooler temperatures. On the contrary, when the model is cooled with liquid nitrogen the free-stream flow is warmer than the surface and a turbulent boundary layer appears as a region of higher temperatures.

Compared to the techniques mentioned in Sect. 2.1, IRT can be used for quantitative surface temperature measure-ments or qualitative flow visualization on a large portion of the model, without the necessity of multiple local mea-surements. If local information is needed, however, data can be retrieved from the whole image using the post-processing software that comes with the most common IR cameras used for scientific purposes. In its simplest and most straightforward use, IRT does not require to paint or spray polymers, liquids or other substances on the model

surface before each run and, thus, cleaning after testing is not needed. The absence of interaction with the model in the wind tunnel is preferable for the study of transition because of the extreme sensitivity of the flow to environmental disturbances through the receptivity mechanism (Saric et al. 2000). Very small scratches, dings, cavities, holes, humps, etc., accidentally produced on the leading edge while interacting with the model surface (spreading of a substance or cleaning) could severely compromise the results. In some cases, if a better image contrast is needed, the model can be heated or cooled so as to change its natural temperature, making IRT more intrusive. In any case, IRT is by far less intrusive than any technique previously described. Since external light sources (such as UV or others) are not necessary, the set-up and the data acquisition system are very simple and compact (only the IR camera and a laptop for its control are needed), making IRT highly portable. For this reason it can be used in different wind tunnels or even for in-flight tests. Moreover, the user does not need to perform the calibration because it is done and certified directly by the vendor and can be checked once in a year.

3 Experimental set-up

3.1 The Supersonic Wind Tunnel

The experiments were carried out at the ASU 0.2-m Supersonic Wind Tunnel, which is a blow-down-to-atmosphere facility with a test-section size of 0.20 m × 0.18 m and nozzle blocks for Mach 2.4, 3.0 and 3.5. The reservoir pressure is 3.45×10^6 Pa (500 psia). When the $M = 2.4$ blocks are used, the tunnel can be started with a settling-chamber pressure of 2.74×10^5 Pa (25 psig), corresponding to a unit Reynolds number $Re' = 28.5 \times 10^6$ m^{-1} ($Re' = 8.7 \times 10^6$ ft^{-1}). At $M = 2.4$ the wind tunnel has been operated up to a settling-chamber pressure of 5.15×10^5 Pa (60 psig), with unit Reynolds number over $Re' = 50 \times 10^6$ m^{-1}. A schlieren imaging system (which can function in a shadowgraph mode too) is used to visualize shock and expansion waves in the test section.

The facility is equipped with devices aiming at improving the flow quality. Possible wind-tunnel sources of disturbances include entropy fluctuations (i.e. temperature spottiness), vorticity fluctuations, sound and particulates. Entropy fluctuations are traceable to the settling chamber and farther upstream. In the present tunnel, a serpentine pipe system (40 m long) connects the reservoir to the control valves in order to assure a more uniform flow temperature. Moreover, at the entrance of the settling chamber (diameter $d = 0.61$ m) there are four 30-mesh turbulence-reduction screens each of which has an open area ratio of 65%. These turbulence-reduction screens reduce velocity gradients assuring the control of vorticity fluctuations. Acoustic disturbances, on the other hand, should not be critical at the low Mach number $M = 2.4$. Unsteady sound fluctuations, in fact, can originate from the turbulent boundary layer on the walls of the test section or may be radiated from the nozzle. The magnitude of this noise, however, increases with the fourth power of the Mach number, and thus the effect of sound is much worse in hypersonic facilities (Schneider 2001) and can be an issue for $M > 2.5$ (Pate and Schueler 1969). Particulates are the last possible source of disturbances and represent a quite common problem. Even though the low-speed effects are understood, little is known for high-speed configurations (Schneider 2001). In order to avoid contamination by particles or water droplets, 1 μm particle filters are present in the settling chamber of the ASU supersonic facility and a water filter assures dry air. The filter is along the pipe between the compressors and the reservoir. No heaters are used. After the settling chamber, a circular-to-rectangular transition contracts the flow into the subsonic portion of the 2-D convergent–divergent nozzle. Two nozzle blocks form the upper and lower contours of the supersonic nozzle and provide the rectangular test section which has access ports for the installation of the model and instrumentation.

In order to check the flow quality, preliminary tests were carried out on a 7° sharp cone made of Bakelite® (Saric and Reed 2002). In the case of uncooled model, transition occurred at $Re_x = 3 \times 10^6$ for $M = 2.4$. When the model was cooled with liquid nitrogen, transition occurred at $Re_x = 3.2 \times 10^6$. These transition Reynolds numbers are not the best and indicate that this tunnel has modest free-stream-sound flow quality. However, contrary to streamwise instabilities, crossflow instability is not sensitive to 2-D roughness or freestream sound. This was proved by extensive studies conducted at the ASU low-speed Unsteady Wind Tunnel by Radeztsky et al. (1999), who found that transition behavior on swept wings is insensitive to sound even at amplitudes greater than 100 dB. The effect of tunnel noise on high-speed crossflow instability remains to be established clearly (Schneider 2001), and for traveling waves there might be some influence of tunnel noise (see Fig. 11 in Schneider 2001, which reports Cattafesta's unpublished work). In the ASU Supersonic Wind Tunnel the noise level is 0.15%. These impact pressure measurements were carried out using a Pitot tube and a microphone. In the case of stationary crossflow instability induced by surface-roughness arrays there is no evidence of sensitivity to sound at high speed, and from low-speed experiments there are good reasons to believe that stationary disturbances are insensitive to sound. Since results presented here are only part of a wider project that aims, as final goal, at controlling stationary crossflow instability in
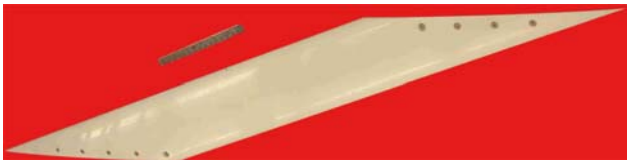
Fig. 1 Aluminum, powder coated model. Flow from *left* to *right*. 73° leading-edge sweep angle, 71.2° trailing-edge sweep angle, 0.349 m streamwise root chord, 0.271 m streamwise tip chord, 0.304 m streamwise mid-span chord, t/c = 4%. Model mounted on *C*-channels

Fig. 2 Brown Bakelite model. Flow from *left* to *right*. 30° leading-edge sweep angle, 18° trailing-edge sweep angle, 0.254 m streamwise root chord, 0.211 m streamwise tip chord, 0.233 m streamwise mid-span chord, t/c = 6%. Model mounted on the sting, in the middle plane of the test section. *Pencil lines* are used as reference

supersonic flows by employing stationary disturbances generated by surface-roughness arrays, the authors believe that the more conventional blow-down supersonic tunnels can be used for these tests, with no need for a "quiet" supersonic tunnel. Of course, if the interest is in streamwise instabilities or blunt-nose effects, then a quiet supersonic facility is mandatory.

3.2 Wind-tunnel models

A symmetric airfoil shape was chosen to minimize the aerodynamic loads in the experiments. Models made of metals and Bakelite® were used. Metals, and in particular aluminum, have a very high thermal conductivity (on the order of 240 W/(m K) for aluminum at 30°C) which makes temperature differences disappear quickly ("wash-out" effect) and hence leads to some difficulties in laminar-to-turbulent transition detection. Therefore, aluminum and steel models were powder-coated with a 76 μm-thick coating (a DuPont® thermosetting epoxy powder designed for various industrial applications) to provide a better insulation between the model and the flow. Nevertheless, the metal models showed some problems, especially related to reflections. Models made of Bakelite® were thus utilized. This material features a very low thermal conductivity, on the order of 0.233 W/(m K), which reduced the "wash-out" effect typical of metal models and gave much less problems related to reflections. Two examples of models are reported here.

In Fig. 1, the aluminum powder-coated model with a 73° leading-edge sweep angle is shown. The root chord in the streamwise direction is 0.349 m (bottom of the figure), the tip chord is 0.271 m, the mid-span chord is 0.304 m (in Fig. 1 the root chord seems shorter than the tip one due to perspective effects of the picture). The trailing-edge sweep angle is 71.2° and t/c = 4%. The attachment-line Reynolds number is $\mathcal{O}(40)$, well below 100 in order to avoid attachment-line contamination. The five holes visible on the root-chord side and the four ones on the tip-chord side are used to fix the model on *C*-channels, which are attached to the wind tunnel.
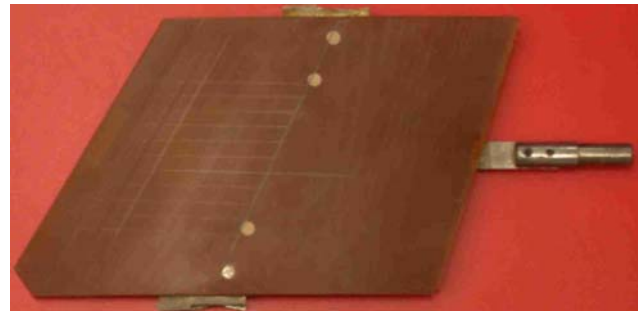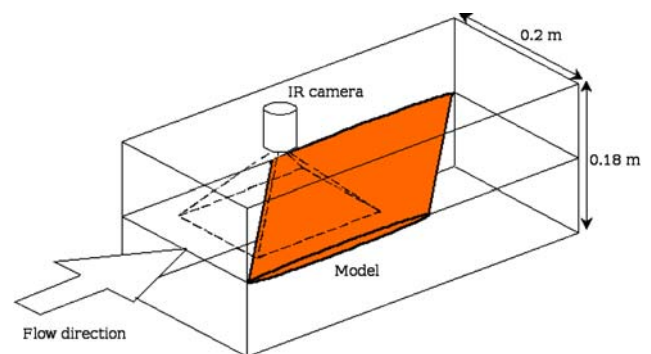

Fig. 3 Sketch of the experimental set-up. In this configuration the wind-tunnel model is set horizontally and in the middle plane of the test section. The IR camera is focused on a rectangular region, which includes the leading edge and part of the upper surface. Flow from *bottom-left* corner to *top-right* (Note that the geometrical dimensions are not respected in the figure)

The 30° swept-wing model made of brown Bakelite® is shown in Fig. 2. The trailing-edge sweep is 18°, the root chord is 0.254 m and the tip chord is 0.211 m. This is the thickest wing tested, with t/c = 6%. The leading edge is supersonic, as for every model with a leading-edge sweep angle smaller than 65.4°. The wing is mounted along the wind-tunnel centerline through a sting from the back and using two lateral supports, as shown in Fig. 2.

Models can be tested vertically or horizontally. The vertical configuration was used to prove that there are no shock waves generated by the leading edge when the sweep angle Λ is greater than 65.4° (the Mach angle for M = 2.4 is 24.6° so the leading edge is subsonic for $\Lambda > 65.4°$). In the horizontal position, which is the typical one (see the sketch of wind-tunnel set-up shown in Fig. 3), two configurations are possible with the model mounted either close to the floor or in the middle of the tunnel, depending on whether IRT or hotwire anemometry is used. When the model is mounted close to the floor, attention is paid to

make sure that there is no aerodynamic interference with the boundary layer developing on the wind-tunnel floor.

3.3 IR equipment and its usage

The IR camera, a FLIR® SC3000 with a spatial resolution of 320 × 240 pixels, is sensitive in the spectral range of 8–9 μm and is cooled to 70 K. It is mounted above the model in a cavity of the wind-tunnel ceiling (see Fig. 3), so as to have the largest possible field of view, and is directly exposed to the model and the flow without an intermediate window. This avoids radiation losses due to the absorption of a window between the model and the camera.

Tests were carried out with the model at ambient temperature, cooled, or heated. Cooling and heating were performed to assure a significant temperature difference between the model surface and the freestream flow, in order to allow a much better detection of laminar and turbulent regions.

Cooling was achieved by spreading liquid nitrogen on the surface of the model already mounted in the tunnel. Because this is a manual operation and because the thickness of the model is not constant with the chord, regions colder than others could be present. This non-uniform temperature distribution, however, does not compromise the detection of transition, whose signature is a steep temperature gradient (on the order of 2–3°C) in a region of almost uniform temperature (see, e.g. Figs. 14, 15).

Heating was obtained by using electric elements set on the model (Joule effect). Also in this case a non-uniform initial temperature distribution could occur. Tests with heated models were attempted following the idea that a high surface temperature should enhance the radiation from the model to the IR camera and, thus, overshadow the reflections from the environment that could compromise the IR image. The radiation detected by the IR camera, in fact, encompasses a contribution Q_ε due to the actual surface temperature and proportional to the emissivity ε, and a contribution Q_ρ, proportional to the reflectivity ρ, caused by environmental heat sources reflecting on the model. If $Q_\varepsilon \gg Q_\rho$ the IR image should provide a reliable temperature field, almost unaffected by reflections from the surrounding environment. The heating elements, however, did not give very good results as far as resolution of small temperature differences is concerned. For this reason, cooling with liquid nitrogen was extensively employed.

Ambient-temperature tests, in general, produced results very close to hot-model tests because the ambient temperature is usually about 21°C or higher, while the flow temperature during the run is always below 15°C. The stagnation temperature and the initial surface temperature of the model are different for each run and therefore they do not allow a systematic comparison. On the contrary, the crucial information is whether the flow temperature is higher or lower than the surface temperature of the model at the beginning of the run.

An approximate range of the initial model temperature is between –40 and –20°C for cold runs, between 70 and 90°C for hot runs and between 18 and 25°C for ambient runs. In all cases, the stagnation temperature ranges between 20 and 40°C, depending on the time of the day and the time of the year.

4 Problems encountered when using IRT

The air in the cavity where the camera is set is much warmer than the flow in the test section because the heat generated by the IR camera while operating is not easily dissipated. This heat contributes to Q_ρ (the radiation reflected by the model) in a misleading way, causing serious problems in interpreting the IR images. Moreover, Q_ρ is proportional to the reflectivity of the material, which depends on the conditions of surface under investigation. In our case, the latter is required to be very smooth and polished to avoid undesired and unexpected transition due to surface roughness. Therefore, very well polished, metal models cause an IRT image with an artificial hot region due to the high reflectivity coefficient of the surface.

Figure 4 presents a typical situation where environmental reflections dominate and make the test not very useful because of their contamination. The 73° swept-wing aluminum model was cooled with liquid nitrogen before the run. Flow conditions are $M = 2.4$, $Re' = 31.8 \times 10^6$ m^{-1}, flow from left to right. The warmer region in the center of the image is the reflection of the cavity where the camera is located. The cold region behind the 50% chord line is due to a non-uniform temperature distribution that might occur when the model is cooled with liquid nitrogen. The cold spot almost in the center of the image is the reflection of the camera detector, which is at very low temperature. A large roughness element is located close to the leading edge in order to trip the boundary layer and help to understand whether the flow is laminar or turbulent. In fact, a turbulent wedge, generated by a wall disturbance, spreads in the laminar region with an angle on the order of 6°–10°, whereas a turbulent wake behind a roughness element located in a turbulent region is very straight and aligned with the streamlines of the inviscid flow. On the other hand, it is true that non-spreading wake-like or vortex-like features can sometimes be seen in a flow that is almost certainly laminar (Matsumura et al. 2003). The fact that in Fig. 4 the wake behind the roughness element does not spread as a turbulent wedge is a good indication that the flow is most likely turbulent, even close to the leading
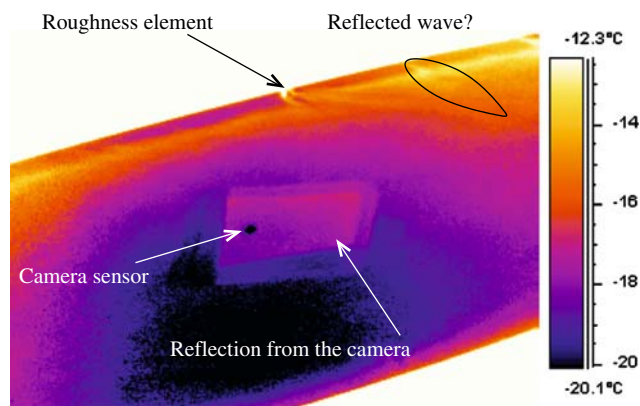
Fig. 4 73° swept-wing aluminum model. $M = 2.4$; $Re' = 31.8 \times 10^6$ m^{-1}; cold run. Flow from *left* to *right*
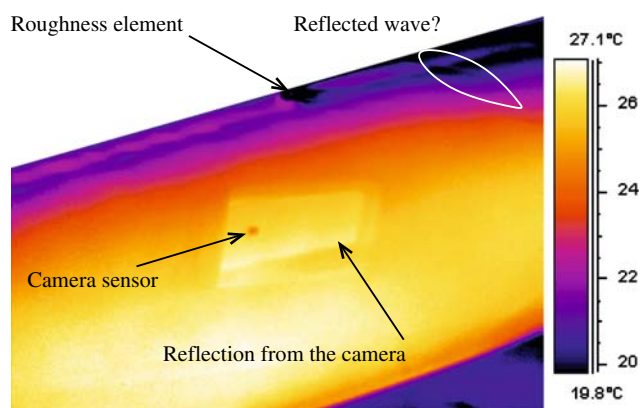

Fig. 6 73° swept-wing phenolic model. $M = 2.4$; $Re' = 31.2 \times 10^6$ m^{-1}; $\alpha = 0°$; ambient run. Flow from *left* to *right*

Fig. 5 73° swept-wing aluminum model. $M = 2.4$; $Re' = 31.8 \times 10^6$ m^{-1}; warm run. Flow from *left* to *right*

Fig. 7 68° swept-wing phenolic model. $M = 2.4$; $Re' = 31.2 \times 10^6$ m^{-1}; $\alpha = 0°$; ambient run. Flow from *left* to *right*

edge. A reflected wave seems to appear, possibly the Mach wave originating from the leading edge at the wing root and then reflecting on the opposite wind-tunnel wall. Figure 5 is a test at the same flow conditions as Fig. 4, but the model is now heated instead of cooled. The reflection from the cavity seems to be weaker compared to Fig. 4. A strongly non-uniform temperature distribution is, however, still present due to the non-uniform action of the heating elements and to the heat losses that are predominant where the thickness of the model is smaller, i.e. at the leading and trailing edges.

Some of the problems related to reflections can be reduced by setting the camera in such a way that its line-of-sight is not perpendicular to the surface. The use of models made of other materials, such as Bakelite® instead of aluminum, significantly improved the reflection issue.

Another typical problem of IR investigations is the knowledge of the emissivity of the surface. In principle it should be measured because it depends on several factors. For our tests, since we are more interested in temperature
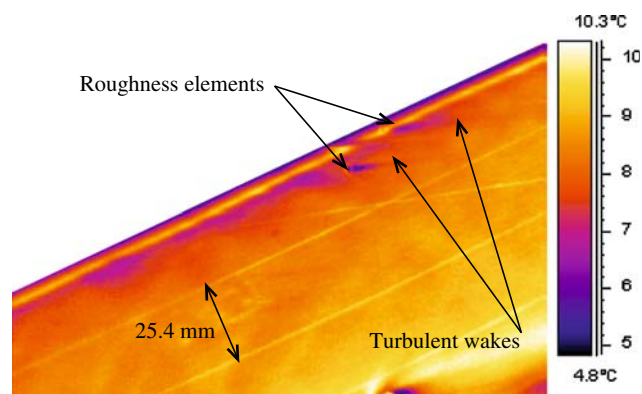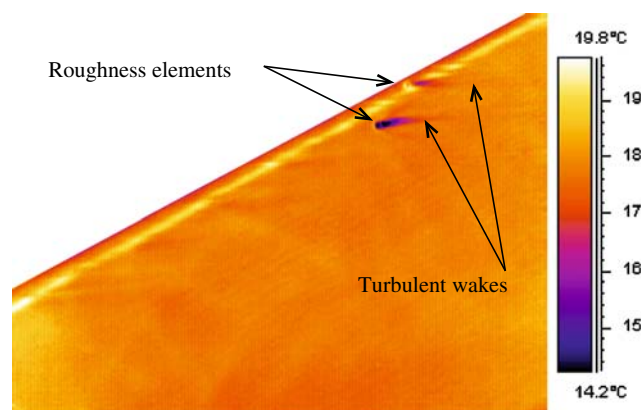
gradients (difference between regions on the surface), rather than in the absolute temperature, the emissivity is not a critical parameter and is assumed to be the tabulated value for that particular material (0.93 for Bakelite®). A posteriori checks demonstrated that an error of 50% in the value of the emissivity changes the temperature values but does not change the position of the temperature gradients, on which transition detection is based.

5 Results and their discussion

We present results obtained only with phenolic (Bakelite®) models because they were not affected by the problem of environmental reflections. In Figs. 6, 7, 8, 9, 11, 12, 13 and 14 the sweep angle changes but the leading edge contour in the plane perpendicular to the leading edge is always the same. Of course, the projection of the leading-edge contour in the direction of the asymptotic flow changes accordingly. Figures 10 and 15 report results referred to a different leading edge. Our goal is to show the effect of
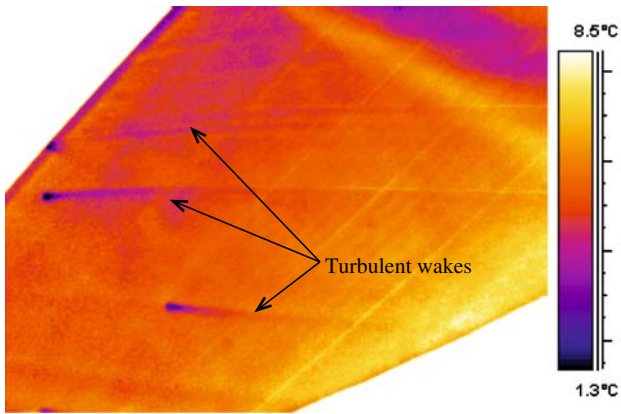
Fig. 8 45° swept-wing phenolic model. $M = 2.4$; $Re' = 31.2 \times 10^6$ m^{-1}; $\alpha = 0°$; ambient run. Flow from *left* to *right*
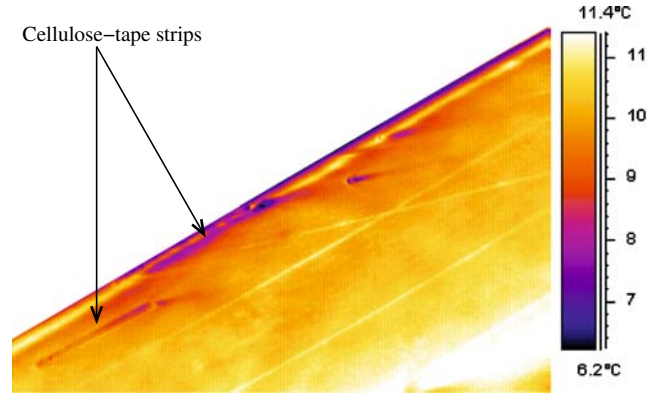

Fig. 11 73° swept-wing phenolic model. $M = 2.4$; $Re' = 31.2 \times 10^6$ m^{-1}; $\alpha = 0°$; celluloid strips; ambient run. Flow from *left* to *right*

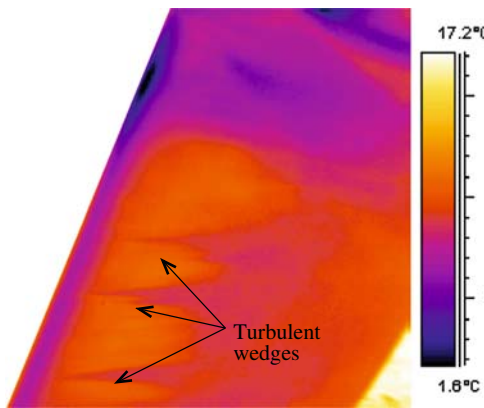**Fig. 9** 20° swept-wing phenolic model. $M = 2.4$; $Re' = 31.2 \times 10^6$ m^{-1}; $\alpha = 0°$; ambient run. Flow from *left* to *right*
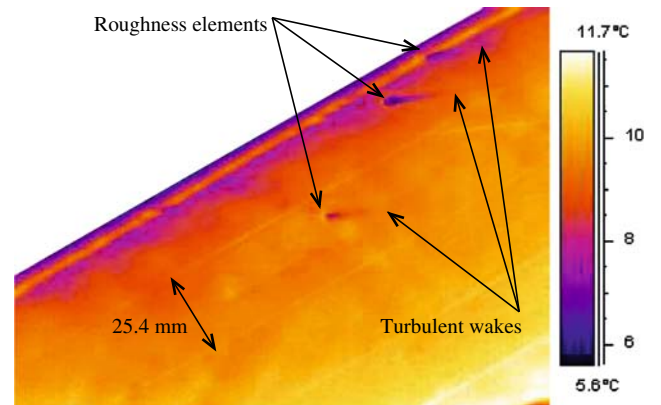

Fig. 12 68° swept-wing phenolic model. $M = 2.4$; $Re' = 31.2 \times 10^6$ m^{-1}; $\alpha = -2°$; ambient run. Flow from *left* to *right*
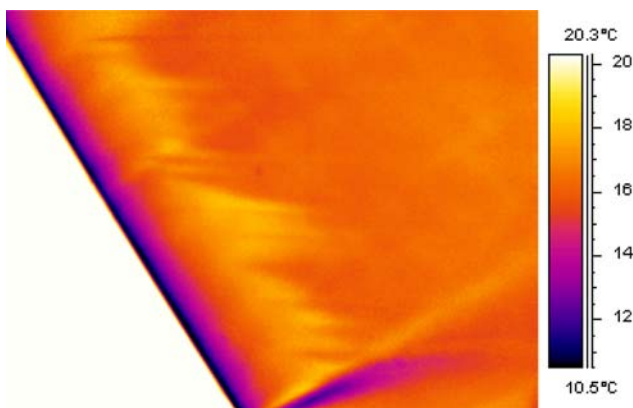

Fig. 10 30° swept-wing phenolic model. $M = 2.4$; $Re' = 29.4 \times 10^6$ m^{-1}; $\alpha = 0°$; ambient run. Flow from *left* to *right*
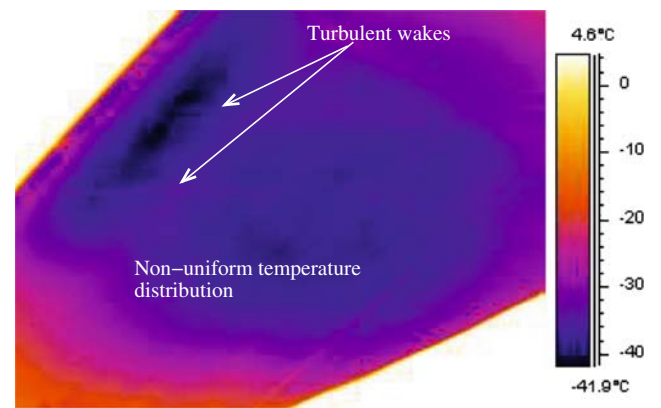

Fig. 13 45° swept-wing phenolic model. $M = 2.4$; $Re' = 31.2 \times 10^6$ m^{-1}; $\alpha = 0°$; cold run. Flow from *left* to *right*

sweep angle, to understand some flow phenomena, and to prove the enhanced potential of IRT when the model is cooled with liquid nitrogen.

Results for the 73° sweep angle model are shown in Fig. 6 for $\alpha = 0°$ (α being the angle of attack), $M = 2.4$ and $Re' = 31.2 \times 10^6$ m^{-1}. Two large isolated roughness
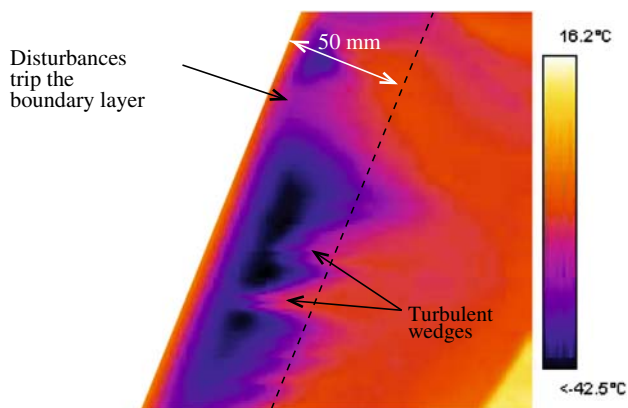
Fig. 14 20° swept-wing phenolic model. $M = 2.4$; $Re' = 31.2 \times 10^6$ m^{-1}; $\alpha = 0°$; cold run. Flow from *left* to *right*
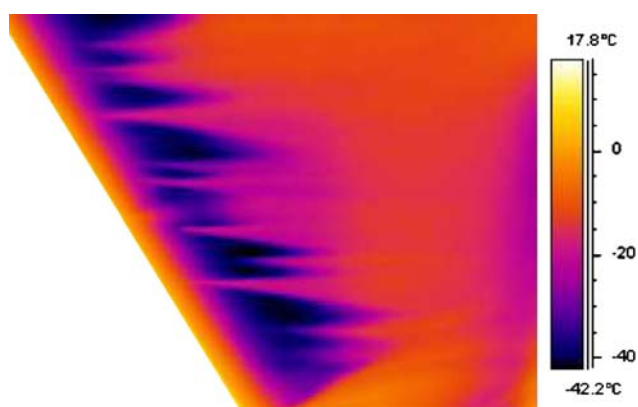

Fig. 15 30° swept-wing phenolic model. $M = 2.4$; $Re' = 29.4 \times 10^6$ m^{-1}; $\alpha = 0°$; cold run. Flow from *left* to *right*

elements are set on the wing in order to visualize whether the boundary layer is laminar or not. They are about 0.7 mm high and have a diameter of about 1.5 mm. The narrow and straight wakes originating from them reveal the presumably turbulent nature of the flow. Some pencil lines parallel to the leading edge were drawn on the surface for reference purpose. An interesting feature that appears on the IR image is a very narrow and elongated region, parallel to the leading edge and located in its proximity, similar to a straight line but slightly wider than the pencil lines visible in the figure, that looks warmer than the surrounding flow. Due to these characteristics, we will refer to it as a "warm line". Such a line could be the signature of some type of transition mechanism (one of the four described in Sect. 2, not necessarily due to crossflow instabilities) or related to a separation bubble. The fact that the warm line is not visible when the wind tunnel is not operating excludes the possibility of being due to optical effects (e.g. reflections).

Results obtained by reducing the sweep angle Λ to 68° are reported in Fig. 7, which refers to $\alpha = 0°$ and to

the same flow conditions as in Fig. 6 ($M = 2.4$ and $Re' = 31.2 \times 10^6$ m^{-1}). $\Lambda = 68°$ was chosen because it is slightly greater than the sonic limit, 64.5°, and should still ensure a subsonic leading edge. Even though the sweep angle is different, results look very similar to those in Fig. 6. When the sweep angle decreases, however, the warm line moves slightly downstream, i.e. further away from the leading edge.

If the sweep angle is decreased to 45°, a value well below the sonic limit, results are as in Fig. 8. Straight wakes originating from the isolated roughness elements suggest that the whole flow field is turbulent, as for larger sweep angles, even though decreasing the sweep angle should increase the area of laminar flow.

A clear transition front is eventually detected at $\Lambda = 20°$, as reported in Fig. 9 ($\alpha = 0°$, $M = 2.4$ and $Re' = 31.2 \times 10^6$ m^{-1}). Since the external flow is at a lower temperature than the model, and the laminar boundary layer is a good insulator, the laminar region appears warmer (about 12°C) than the turbulent one (about 8°C). The transition front is visible at about 50 mm from the leading edge, i.e. approximately 8.5% of the chord, but is not very uniform because of the presence of turbulent wedges originating from very small disturbances on the leading edge. These roughness disturbances were unwanted and were not intentionally set on the wing. On the contrary, the leading edge was polished before the run in order to eliminate them as much as possible. Different runs performed without re-polishing the model revealed that the turbulent wedges are always located in the same positions, while re-polishing the model before the run caused them to move to other positions. A reflected wave is also visible in the upper-right portion of the image, together with an anticipated transition region. The leading edge is much colder than the rest of the model not because of turbulent flow, but simply because of its very low thermal inertia, which lets it reach the external, lower temperature much faster than the rest of the model.

As opposed to Figs. 6, 7, 8 and 9, which featured the same leading edge contour in the plane normal to the leading edge, Fig. 10 reports the result for a 30°-swept wing made of phenolic with a larger leading-edge radius. Conditions are $\alpha = 0°$, $M = 2.4$, $Re' = 29.4 \times 10^6$ m^{-1}, flow from left to right. The transition front is not regular, but it can be located at about 32 mm from the leading edge, corresponding to about 18% of the mean chord. As already learned from the previous figures, for an ambient run the laminar region appears warm and the turbulent one cold. The leading edge is colder than the rest of the wing because of its small thickness; the fact that the isothermal lines in this region are parallel to the leading edge confirms it.

Results presented so far pose two questions. What is causing the warm line that occurs in the proximity of the

leading edge at high sweep angles, and why does the transition front appear clearly only for small values of the sweep angle?

The test reported in Fig. 11 shows the effects of two cellulose tape strips on the model, with the purpose of understanding the origin of the warm line. They are approximately 0.5 mm high, 2.1 mm wide and 40 mm long. The lower one is placed downstream of the warm line, in a presumably turbulent region. If the flow is laminar, the expected effect of the strip would be to cause transition to turbulence. The fact that the lower cellulose strip does not produce sensible changes in the flow on the model, however, corroborates the conjecture of a possible turbulent flow downstream of the warm line. The upstream strip, on the contrary, produces a sort of interruption of the characteristic warm line. This is a further indication that the warm line must be related to aerodynamic effects. One might argue that the interruption in the proximity of the upstream strip could be caused by changes in the emissivity or by the insulating properties of the cellulose strip. The first possibility is excluded by the fact that the strips could not be identified on the IR image when the wind tunnel was not operating. Different insulation caused by the strips would produce a more visible effect on the downstream strip, but this is not the case. These facts lead to the conclusion that the warm line close to the leading edge probably originates from the aerodynamics in that area and is not related to reflections or other spurious phenomena along the visual path.

Changing the angle of attack from $\alpha = 0°$ to $\alpha = -2°$ did not cause changes in the results. By comparing Fig. 12 at $\alpha = -2°$ with the same case at zero incidence (Fig. 7) one can notice that pitching down the model did not change the position of the warm line, contrary to what one could have expected.

From the results it can be concluded that the warm line is probably due to a separation bubble and not to one of the transition phenomena previously described (see Sect. 2). In fact, it cannot be caused by Tollmien–Schlichting waves because of the favorable pressure gradient and in the vicinity of the leading edge. Görtler instability is excluded because of the surface convex curvature. Attachment-line contamination cannot occur because the attachment-line Reynolds number expressed as a function of leading edge curvature radius and sweep angle (Pfenninger 1977; Poll 1985; Reed and Saric 1989) is on the order of 40. This respects the criterion (Reed and Saric 1989; Saric and Reed 2004) stating that, if the attachment-line momentum-thickness Reynolds number is below 100, wing-root disturbances are prevented from propagating along the attachment line and feeding into and tripping the boundary layer. This was also proved by comparing tests carried out with the wing root mounted

close to or far away from the wind-tunnel wall. In the first case the disturbances present in the turbulent boundary layer developing on the tunnel wall could have propagated along the attachment line, whereas in the second case this would not have been possible. Since results did not change depending on the configuration, attachment line contamination can be excluded. The fact that the warm line is very straight excludes also crossflow instability, the last possible "classical" mechanism, which rarely presents uniform characteristics as a function of spanwise coordinate. The presence of a separation bubble explains the fact that the line is straight and parallel to the leading edge and the fact that it disappears as the sweep angle decreases. In the latter conditions, in fact, the pressure gradient becomes steeper at the leading edge, preventing the boundary layer from separating in a bubble with turbulent reattachment. Similar experiments carried out on a similar model at the NASA-LaRC UPWT showed a leading-edge separation bubble that tripped the flow (Saric and Reed 2004).

The second question, regarding the reason why a clear transition front is visible only at low sweep angles, can be answered by recalling that a low sweep angle causes a weak crossflow so that an instability, possibly induced by the crossflow, is weak and allows a laminar region in the proximity of the leading edge. A second explanation could be that a lowered sweep angle makes the subsonic region around the leading edge become smaller, preventing the environmental disturbances from propagating upstream and/or tripping the boundary layer.

A final set of results is presented for cold runs in order to show the effect of the initial model temperature relative to the external flow.

Figure 13 reports the IR image for the 45° sweep-angle model and refers to the same flow conditions as Fig. 8. Also in this case the leading edge features a small region of reversed temperature, which is not due to transition but to its low thermal capacity. The presence of warmer spots that irregularly interrupt the cold region close to the leading edge (Fig. 13) suggests possible laminar flow in the proximity of the latter. These spots resemble turbulent wedges originating from surface roughness on the leading edge and developing in a laminar region, as seen in Figs. 9 and 10. A clear transition front, however, cannot be identified and a definite conclusion cannot be drawn from Fig. 13.

Figure 14 refers the 20° swept-wing phenolic model cooled with liquid nitrogen (same conditions as in Fig. 9). The transition front is now visible, as expected by considering the effect of sweep angle seen in Figs. 6, 7, 8 and 9, but because the model was cooled with liquid nitrogen before the run instead of being at ambient temperature, colors are reversed. Now the transition front corresponds to temperature gradients from cold to warm. Transition

detection is enhanced and much clearer in cold conditions rather than in ambient runs.

In Fig. 15 a cold run is shown for the 30° swept-wing phenolic model at the same conditions as Fig. 10 (the leading edge radius is different from Figs. 13 and 14). The transition front is still at the same location as for the ambient run, but some details, such as the shape of the turbulent wedges and their locations, are clearly different because the wing surface was re-polished between the two runs. The laminar region is cold because the initial temperature of the surface was very low. The leading edge is warm because of its low thermal inertia.

Figures 9, 10, 14 and 15 show a clear transition front, but cold runs allow a better contrast and therefore are preferable for transition detection. However, it must kept in mind that cooling with liquid nitrogen can change the stability characteristics as a consequence of the viscosity changes close to the surface. In this sense, a cold run can be considered "intrusive".

6 Conclusions

Boundary-layer transition investigations are carried out on swept wings in supersonic flows ($M = 2.4$) by employing IRT. Transition is clearly visible only for sweep angles below 45°. In all other cases the flow over the wing is almost completely turbulent, as proved by the use of isolated roughness elements which produced effects typical of turbulent flows.

The transition front appears on the thermo-graphic image as a strong gradient (discontinuity) from hot to cold regions or vice-versa, depending upon the initial temperature of the model (respectively warmer or colder than the oncoming flow). This behavior is a direct consequence of the difference in the convective heat-transfer coefficient between laminar and turbulent boundary layers. A laminar boundary layer experiences low heat exchange and acts as an insulator, whereas in a turbulent boundary layer the heat exchange is accelerated. When the model is cooled with liquid nitrogen, i.e. the surface temperature before the run is lower than the external incoming flow, laminar regions are cold and turbulent regions are warm. Transition detection is enhanced when the model surface is colder than the freestream flow.

Results demonstrate that IRT is a very appropriate tool for studying laminar-to-turbulent boundary-layer transition. Its straightforward use and the absence of additional operations required by the other techniques available for transition detection (e.g. modification of the model surface, spreading of substances or extra light sources) make it very portable and suited for both wind-tunnel and in-flight testing.

References

Berry SA, Bouslog SA, Brauckman GJ, Caram JM (1997) Boundary layer transition due to isolated roughness: shuttle results from the LaRC 20-Inch Mach 6 Tunnel. AIAA Paper 97-0273

Blanchard RC, Tietjen A (2000) Infrared sensing aeroheating flight experiment (ISAFE). In: Proceedings of 9th international symposium on flow visualization. Edingburgh, UK

Brandon JM, Manuel GS, Wright RE, Holmes BJ (1990) In-flight flow visualization using infrared imaging. J Aircr 27:612–618

Cattafesta LN, Iyen V, Masad JA, King RA, Dagenhart JR (1995) Three-dimensional boundary-layer transition on a swept wing at mach 35. AIAA J 33(11):2032–2037

Creel TR Jr, Beckwith IE, Chen FJ (1987) Transition on swept leading edge at mach 3.5. J Aircr 24(10):710–717

Deyhle H, Bippes H (1996) Disturbance growth in an unstable three-dimensional boundary layer and its dependence on initial conditions. J Fluid Mech 316:73–113

Green MJ, Budnik MP, Yang L, Chiasson MP (1983) Supporting flight-data analysis for space-shuttle orbiter experiments at nasa ames research center. NASA TM 84345

Hall RM, Obara CJ, Carraway DL, Johnson CB, Wright RE Jr, Covell PF, Azzazy M (1991) Comparisons of boundary-layer transition measurement techniques at supersonic mach numbers. AIAA J 29(6):865–879

Kaplan H (1999) Practical applications of infrared thermal sensing and imaging equipment. 2nd Edition. SPIE Optical Engineering Press, Bellingham, WA

King RA (1992) Three-dimensional boundary-layer transition on a cone at mach 3.5. Exp Fluids 13(5):305–314

Kosinov AD, Semionov NV, Ermolaev YuG, Levchenko VYa (2000) Experimental study of evolution of disturbances in a supersonic boundary layer on a swept wing model under controlled conditions. J Appl Mech Tech Phys 41(1):44–49

Levchenko VYa, Kosinov AD, Semionov NV, Ermolaev YuG (1996) Instability of a three-dimensional supersonic boundary layer. In: Duck PW, Hall P (eds) IUTAM symposium on nonlinear instability and transition in three-dimensional boundary layers. Kluwer, Dordrecht

Liu T, Campbell BT, Burns SP, Sullivan JP (1997) Temperature- and pressure-sensitive luminescent paints in aerodynamics. Appl Mech Rev 50(4):227–246

Maldague X (2001) Theory and practice of infrared technology for non destructive testing. Wiley, New York

Maldague X, Moore PO (2001) Nondestructive testing handbook: infrared and thermal testing. American Society for Nondestructive Testing

Matsumura S, Schneider SP, Berry SA (2003) Flow visualization measurement techniques for high-speed transition research in the boeing/afosr mach-6 tunnel. AIAA Paper 2003-4583

Merski NR (1999) Global aeroheating wind-tunnel measurements using improved two-color phosphor thermography method. J Spacecr Rockets 36(2):160–170

Mielke CH, Kleiser L (1999) Investigation of transition to turbulence in a 3d supersonic boundary layer. In: Fasel HF, Saric WS (eds) Laminar–turbulent transition. Springer, Berlin, pp 397–402. Paper presented at the 5th IUTAM symposium on laminar–turbulent transition, Sedona, USA, 1999

Miley SJ, van Dam CP, Yip LP, Willard PE, Crowder JP, Wazlavick RL (1997) Slat transition characteristics on the NASA B737-100 aircraft using infrared imaging and hot-film anemometry. In: Crowder JP (ed) Flow visualization VII. Begell House, New York, pp 950–956

Morkovin MV (1969) On the many faces of transition. In: Wells CS (ed) Viscous drag reduction. Plenum, New York

Morkovin MV (1985) Bypass transition to turbulence and research desiderata. In: Graham R (ed) Transition in turbines. NASA Conf Publ 2386, 161

Pate SR, Schueler CJ (1969) Radiated aerodynamic noise effects on boundary-layer transition in supersonic and hypersonic wind tunnels. AIAA J 7(3):450–457

Pfenninger W (1977) Laminar flow control—laminarization. In: AGARD Rep. No. 654 (Special course on drag reduction). von Karman Institute, Rhode-St.-Genese, Belgium

Poll DIA (1985) Some observations of the transition process on the windward face of a long yawed cylinder. J Fluid Mech 150:329–356

Quast A (1987) Detection of transition by infrared image technique. In: Proceedings of the ICIASF Record, Williamsburg, VA, June 22–25. Institute of Electrical and Electronics Engineers, New York, pp 125–134

Radeztsky RH, Reibert MS, Saric WS (1999) Effect of isolated micron-sized roughness on transition in swept-wing flows. AIAA J 37(11):1370–1377

Reed HL, Saric WS (1989) Stability of three-dimensional boundary layers. Ann Rev Fluid Mech 21:235–284

Reed HL, Saric WS, Arnald D (1996) Linear stability theory applied to boundary layers. Ann Rev Fluid Mech 28:389–428

Saric WS (1994) Görtler vortices. Ann Rev Fluid Mech 26:379

Saric WS, Reed HL (2002) Supersonic laminar flow control on supersonic wings using distributed roughness. AIAA Paper 2002-0147

Saric WS, Reed HL (2004) Toward practical laminar flow control—remaining challenges. AIAA Paper 2004-2311

Saric WS, Reed HL, Kerschen EJ (2000) Boundary-layer receptivity to freestream disturbances. Ann Rev Fluid Mech 34:291–319

Saric WS, Reed HL, White EB (2003) Stability and transition of three-dimensional boundary layers. Ann Rev Fluid Mech 35:413–440

Schneider SP (2001) Effects of high-speed tunnel noise on laminar–turbulent transition. J Spacecr Rockets 38(3):323–333

Semisynov AI, Fedorov AV, Novikov VE, Semionov NV, Kosinov AD (2003) Stability and transition on a swept cylinder in a supersonic flow. J Appl Mech Tech Phys 44(2):212–220

van Dam CP, Shiu HJ, Banks DW (1998) Remote in-flight boundary layer transition visualization using infrared thermography. In: Proceedings of 8th international symposium on flow visualization. Sorrento, Italy